RADAR SCATTERING LAWS AND WAVELENGTH DEPENDENCE OF THE LUNAR SURFACE

Richard A. Simpson
Center for Radar Astronomy
Stanford, CA 94305

26 January 1978

This research was supported by NASA grant NSG 7029. The Center for Radar Astronomy is operated with partial support from NASA Grant NGL 05-020-014.

ABSTRACT

Data from Apollo lunar bistatic radar experiments have been processed to give probability density functions for surface slopes. These show best agreement with a Hagfors scattering law, though data having both gaussian and exponential characteristics also exist. Surface roughness estimates range from 4° in maria to at least 8° in highlands, values which are appropriate to 25 m horizontal scales and which are areal averages over tens of square kilometers. Roughness varies with wavelength, most strongly in maria.

INTRODUCTION

Dual frequency bistatic-radar observations of the moon have been made using the Apollo 14, 15, and 16 spacecraft in lunar orbit. Transmissions from the command-service modules were received on earth after reflection from the lunar surface. Modulation on the signals, which resulted from interaction of the electromagnetic wave with the surface, can be analyzed to give information about the latter's properties. In this report we discuss probability density functions for surface slope which have been obtained from these data.

The geometry and operational aspects of this experiment have been discussed in detail elsewhere (Tyler and Howard, 1973). Theoretical background on the radiowave scattering problem has been developed by Tyler and Ingalls (1971). Methods for obtaining the slope density functions from the resultant radar echo spectra have been outlined by Parker and Tyler (1973); Lipa and Tyler (1976) have applied these techniques to Mars radar data.

Apollos 14 and 15 provided data at both 13 and 116 cm wavelengths; only 13 cm was available from Apollo 16. Slope density functions were obtained on two degree longitudinal centers along approximately equatorial ground tracks. The experimentally derived functions have been compared with theoretical expressions and have been examined for wavelength dependence. A brief review of the background and a summary of the results follows.

EXPERIMENT

In a bistatic-radar experiment, such as the one conducted here, the signal originates at a spacecraft,moving with velocity $\overline{V}_{sc}$. The incoming wave interacts with the surface, which behaves like a polished (but not perfectly smooth) sphere. Scattering at radio frequencies is locally specular so that most energy reaching the receiver arrives from a region near the point on the mean sphere where angle of incidence equals angle of reflection. As the spacecraft moves, so does the primary reflection region and over a period of time a track is defined across the surface. Spacecraft motion also causes the echo to be broadened because of differential Doppler offsets at each reflection point within the primary region.

Our scattering model is based on the assumption that the echo arises from specular scattering by those parts of a gently undulating surface which are oriented so as to reflect energy toward the receiver. The dimensions of the scattering elements are believed to be in the range of one to 1000 times the radar wavelength (λ), with an effective size being about 200λ (Tyler et al., 1971). The size of a Fresnel zone (the area over which a reflection may be considered coherent) marks the upper limit of this range; at the small end, scattering passes into the Rayleigh regime. The total echo is the vector sum (to account for both amplitude and phase) of the individual contributions. Its frequency dispersion is a measure of the surface roughness.

Scattering facets away from the specular point will contribute less in proportion to their probability of being oriented for mirror-like reflection. Each contribution to the echo will be Doppler shifted in frequency by an amount which is proportional to the scalar product between the look vector towa

the facet, $\hat{u}_a$, and $\overline{V}_{sc}$. Loci of constant Doppler shift are found to be along the intersection of a cone defined by $\hat{u}_a \cdot \overline{V}_{sc}$ = constant and the planetary sphere (Tyler and Ingalls, 1971). One can estimate the received signal at any frequency by combining this geometrical knowledge with a postulated distribution of reflecting facets.

For this work we will describe facets in terms of their tilt θ with respect to the mean spherical surface. The angle θ is indeperdent of azimuth and is give by, $\theta = \arccos(\hat{n} \cdot \hat{u}_r)$, where $\hat{n}$ is the unit normal for a facet and $\hat{u}_r$ is the unit normal (radial) to the mean sphere. Any facet for which the above condition holds becomes part of the distribution $p(\theta)$ but only those facets for which angle of incidence equals angle of reflection contribute to the echo.

The expression for power spectral density in the received echo $w(f)$ may be separated into two parts if one makes reasonable assumptions (Parker and Tyler, 1973). The function $H(\bar{r},\bar{s})$ depends solely on experimental geometry, while $p(\theta)$ describes the distribution of roughness. Together, they give

$$w(f) = \int H(\bar{r},\bar{s})\ p(\theta)\ d\theta$$

where the integration is performed over that part of the surface which is mutually visible from transmitter and receiver. The vector $\bar{r}$ is the position of the spacecraft and the vector $\bar{s}$ is the position of the specular point.

If a data spectrum $W(f)$ is given, it becomes possible (after invoking appropriate assumptions) to invert the computation to obtain $P(\theta)$, an experimental slope distribution. In performing the inversion, one assumes that the scattering surface is homogeneous over the strips which contribute to

individual frequency bins; there are no à priori assumptions about the form of $P(\theta)$, however, so the result should be an accurate description of the surface. In our analysis we have compared experimentally determined $P(\theta)$ with theoretical expressions $p(\theta)$.

ANALYSIS

The inversion techniques of Parker and Tyler (1973) were applied to 13 cm wavelength data from each of the three Apollo spacecraft and to 116 cm data from Apollos 14 and 15. The resultant slope density functions have been compared with three theoretical expressions. Background and information on their applicability are contained in the Appendix.

The Gaussian law

$$p_G(\theta) = (\sec^3\theta/\tan^2\theta_o) \exp(-\tan^2\theta/\tan^2\theta_o)$$

is mathematically convenient, allows for calculation of $\tan^2\theta$ in closed form, and has been widely used in theoretical treatments of scattering (see Beckmann and Spizzichino 1963).

The exponential law,

$$p_E(\theta) = A \exp(-\tan\theta/\tan\theta_o)$$

does not have the mathematical advantages of the gaussian, but its intrinsic properties make it a good alternative to the first distribution. Its use in scattering studies follows from substitution into the results of Kodis (1966).

The third law, derived by Hagfors (1964),

$$p_H(\theta) = B \cos\theta \, (\cos^4\theta + C \sin^2\theta)^{-3/2}$$

has theoretical limitations (Barrick, 1970) but agrees well with planetary radar experiments (Evans and Hagfors, 1968). Points central to its deviation, a gaussian surface height distribution and an exponential surface anticorrelation function, appear to hold for at least some earth surfaces (Hayre and Moore, 1961).

Our comparison of data with the above theoretical expressions was simply through consideration of squared error

$$\varepsilon^2 = \sum_{i=1}^{20} \left| P(\theta_i) - K' p(\theta_i) \right|^2 \sin\theta \, \Delta\theta \qquad \Delta\theta = 1.0°$$

K' is computed analytically for best fit, and one adjusts the characteristic surface roughness ($\tan\theta_o$ or C, depending on the law) to obtain minimum ε^2.

RESULTS

Results of the comparisons are shown in Fig. 1 for Apollo 15 data at 13 cm wavelength. Fig. 1a shows $\log_{10}(\varepsilon^2)$ for the three theoretical density functions while the lower plot gives the rms surface roughness which one would derive from the best fit Hagfors distribution $p_H(\theta)$ (see Appendix). For the most part, the Hagfors law (solid line in Fig. 1a) provides the best agreement with the data. Beyond about 50° longitude (both east and west) all three laws show noticeably higher fit error because of noisier data.

In maria the Hagfors and exponential laws, both of which have non-negligible tails, are clearly superior to the gaussian. In highlands, the situation is less clear, with all three laws showing similar fit errors. From a subjective point of view, the fits in highlands do not appear so good as those in maria; the normalization procedure used (see Appendix) causes the numerical values

for square error to be virtually the same, however.

The upper limit of roughness values (about 8°) shown for highlands in Fig 1b may be an artifact of argument truncation in the experimental slope density functions; only probabilities for slopes between $\theta = 0°$ and $\theta = 20°$ were obtained in the inversion process. It may be that highland areas have rms slopes greater than 8°, but that these cannot be determined unless the range of θ is extended. Certainly significant tilts at angles larger than $\theta = 20°$ would materially alter the rms surface slope estimate.

The apparent indifference of the fitting procedure to scattering law in highland areas may also be an artifact of the θ truncation. For the larger values of rms roughness, the tails of all density functions fall outside the $\theta = 20°$ limit. Since the absence of a tail appears to be what distinguishes the gaussian from the Hagfors and exponential laws in maria, the more favorable values of ε^2 for the gaussian determined using the broad density functions is not surprising.

Fig. 2 shows examples of data which match, under the truncation conditions noted above, each of the three theoretical expressions considered. Error bars refer to uncertainty in the inversion process; solid lines are best-fit theoretical curves. For the most part, the Hagfors law was the preferred theoretical expression, but, as can be seen, the exponential (and occasionally the gaussian) sometimes provided the best fit.

The data were grouped into the broad classifications of maria and highlands for further study. This differentiation was based on a subjective study of very low resolution lunar photography; mountainous terrain was considered highlands and the large plains were labeled maria. Since each data point represents an average response over two degrees of longitude along the groundtrack, it was impossible in some cases to arrive at an unambiguous classification. Scattering areas which included both mountains and plains or which could not be simply classified as one or the other, were labeled

"transition" regions. The breakdown for data obtained along the Apollo 15 ground track is given in Table I.

Data points were then plotted on a three variable "phase diagram" such as that shown in Fig. 3. The distance from any vertex depends on the error incurred during fitting of the data points to the theoretical curve. For small Hagfors errors (E_H^2) relative to exponential and gaussian, for example, D_H will be less than either D_E and D_G and so the data point will be closest to the Hagfors vertex of the triangle. In this way, one can determine the relative importance of Hagfors, exponential, and gaussian characteristics in any given set of data.

The actual Apollo 15 13 cm points are given in Fig. 4. One should note the high percentage of points within the Hagfors third of the phase diagram. Also, in two-way comparisons, such as the histograms along each of the edges illustrate, the Hagfors law shows a definite preference over either the exponential or the gaussian. Along the bottom edge, where the gaussian and exponential laws are compared independently of the Hagfors, the exponential is favored.

By separating the data into terrain types, as per Table I, one can generate phase diagrams and histograms for mare and highland points separately. These show an extreme prejudice against the gaussian law when the mare data are used exclusively (Fig. 5). In fact when Apollo 16 mare points are plotted in the same way (not shown here), no data appear on the left hand side of the diagram at all. The distinction between Hagfors and exponential properties in maria is less clear, though there is some skewing toward the former.

When highland points are used exclusively, the preference is toward Hagfors characteristics in two-way comparisons (Fig. 6), but the trends

are less strong than with mare data. On the gaussian-exponential side of the diagram, there is no clear pattern. There are fewer highland points than mare points, so the significance of these latter conclusions must be less. Further, the scatter of the highland points suggests that many more would be needed in order to draw strong conclusions. The entire highland analysis is intertwined with the truncation problem discussed earlier. It may be that with better and more abundant data the apparent drift from Hagfors toward gaussian properties in highlands will turn out to be simply an artifact of the 20° cutoff in probability density function determination. More data are clearly needed before these questions can be finally answered.

One should note in Figs. 4 and 5 that there are very few data points within the interior triangle defined by the gaussian and exponential vertices and the midpoint of the triangle. This suggests that the Hagfors law is indeed a good compromise between the gaussian and exponential versions. The rounded peak and the non-negligible tails which characterize the Hagfors law make it good for transition between the two more extreme expressions. The fact that most of the data fall within the "compromise" range rather than toward either or both extremes indicates that we have adequately covered the range of scattering law possibilities.

Though not shown here, the Apollo 14 and 16 13 cm data (of lower and higher signal-to-noise ratio, respectively, than Apollo 15) are in excellent agreement with these conclusions.

The VHF data have been analyzed in exactly the same way as the 13 cm results. Fig. 7 shows the logarithm of squared error and estimated rms surface slope for the Apollo 15 ground track at 116 cm wavelength. Rms surface slopes in the western maria are typically 2°, while those in the highlands range to 8°. It is this same 8° apparent upper limit in highlands

which caused concern regarding a possible truncation error in the processing of the 13 cm wavelength data. We thus view conclusions based on these highland results with less certainty than those for maria. Tyler (1978), on the other hand, has found both theoretical and experimental evidence for believing that the change in behavior between maria and highlands is real.

The surface roughness estimates from the 13 and 116 cm data sets (Figs. 1 and 7, respectively) have been compared in Fig. 8. Earlier studies (Hagfors and Evans, 1968; Parker and Tyler, 1973) have shown wavelength dependence in backscatter and, from a limited analysis, wavelength dependence in oblique scatter. The inference from Fig. 8 is that there is a strong wavelength dependence in the scattering process thoughout mare regions. In the western maria the factor of two difference in roughness between 13 cm and 116 cm wavelengths is consistent with a surface roughness (s) variability of form

$$s \propto \lambda^{\alpha}$$

where the exponent α has a value on the order of -0.3. In Montes Apenninus there is no apparent wavelength variation; roughness at both wavelengths appears to be about 6-8° so that α in the above expression would be 0.0. Mare Serenitatis, which appears to have wavelength dependence, but to a lesser degree than the western maria, shows a dependence of approximately $\alpha = -0.2$. A tabulation of the wavelegth results by geographic area is given in Table II. One-sigma error bars represent the variability within the N data points and not the uncertainty in obtaining those points.

REFERENCES

Barrick, D.E., Unacceptable height correlation coefficients and the quasi-specular component in rough surface scattering, Radio Science, 5, 647-654, 1970.

Beckmann, P. and A. Spizzichino, The Scattering of Electromagnetic Waves from Rough Surfaces, Pergamon, New York, 1963.

Evans, J.V. and T. Hagfors, Radar Astronomy, McGraw-Hill, New York, 1968.

Hagfors, T.,Backscatter from an undulating surface with applications to radar returns from the moon, J. Geophys. Res., 69, 3779-3784, 1964.

Hayre, H.S. and R.K. Moore, Theoretical scattering coefficient for near vertical incidence from contour maps, J. Res. of National Bureau of Standards, 65D, 427-432, 1961.

Kodis, R.D., A note on the theory of scattering from an irregular surface, IEEE Trans. on Ant. and Propag., AP-14, 77-82, 1966.

Lipa, B.J. and G.L. Tyler, Surface slope probabilities from the spectra of weak radar echoes: application to Mars, Icarus, 28, 301-306, 1976.

Parker, M.N. and G.L. Tyler, Bistatic-radar estimation of surface-slope probability distributions with applications to the moon, Radio Science, 8, 177-184, 1973.

Tyler, G.L. Comparison of quasi-specular radar scatter from the moon with surface parameters obtained from images, submitted to Icarus, 1978.

Tyler, G.L. and H.T. Howard, Dual-frequency bistatic-radar investigations of the moon with Apollos 14 and 15, J. Geophys. Res., 78, 4852-4874, 1973.

Tyler, G.L. and D.H.H. Ingalls, Functional dependences of bistatic-radar frequency spectra and cross sections on surface scattering laws, J. Geophys. Res., 76, 4775-4785, 1971.

References (cont.)

Tyler, G.L., R.A. Simpson, and H.J. Moore, Lunar slope distributions: comparison of bistatic-radar and photographic results, J. Geophys. Res., 76, 2790-2795, 1971.

APPENDIX

SLOPE DISTRIBUTION FUNCTIONS AND RADAR CROSS SECTION

Several commonly used probability density functions for surface slopes are given. Both unidirectional slope (slope measured along a particular line, such as the x-axis) and adirectional slope (the title of a facet with respect to the normal to the mean surface) are used.

1. Rea, Heatherington, and Mifflin (1964) have defined tilt through

$$dA = p_{RHM}(\theta)\, d\omega$$

where dA is the area of an incremental scattering facet tilted an angle θ with respect to the mean surface normal, and $d\omega$ is the element of solid angle into which the normal to dA points. The quantity $p_{RHM}(\theta)$ is the density function giving the probability that said facet normal is within $d\omega$.

Projected area on the mean surface is

$$dS = \cos\theta\, dA = \cos\theta\, p_{RHM}(\theta)\, d\omega$$

and the normalization requirement is

$$\int_{\text{hemisphere}} dS = \int_{\text{hemisphere}} \cos\theta\, dA = \int_{\text{hemisphere}} \cos\theta\, p_{RHM}(\theta)\, d\omega = 1$$

As the density function is independent of azimuthal angle, the normalization may be rewritten

$$2\pi \int_0^{\pi/2} p_{RHM}(\theta) \cos\theta \sin\theta \, d\theta = 1$$

where $d\omega = \sin\theta \, d\theta \, d\phi$.

Rea, Heatherington, and Mifflin (1965) modified their work somewhat after Hagfors pointed out that $p_{RHM}(\theta)$ was defined with respect to the actual undulating surface rather than to the mean flat surface. A new density function can then be defined

$$p_H(\theta) = \cos\theta \; p_{RHM}(\theta)$$

with normalization

$$2\pi \int_0^{\pi/2} p_H(\theta) \sin\theta \, d\theta = 1$$

2. Muhleman (1964) defined the probability density function $p_M(\theta,\phi)$ where $p_M(\theta,\phi) \, d\omega$ is the probability that a facet normal points into solid angle $d\omega$ at zenith-azimuthal coordinates (θ,ϕ). The proper normalization in this case is

$$\int_0^{2\pi} \int_0^{\pi/2} p_M(\theta,\phi) \sin\theta \, d\theta \, d\phi = 1$$

Usually independence of Ø is assumed so that

$$2\pi \int_0^{\pi/2} p_M(\theta,\emptyset) \sin\theta \, d\theta = 1$$

Parker (1973), following Muhleman, introduced a one-dimensional density function

$$p_p(\theta) = \int_0^{2\pi} p_m(\theta,\emptyset) \, d\emptyset$$

where normalization is according to

$$\int_0^{\pi/2} p_p(\theta) \sin\theta \, d\theta = 1$$

3. Beckmann (1963), among others, began with an analytic expression for the rough surface $\zeta(x,y)$ from which a density function $p_B(\zeta_x,\zeta_y)$ in terms of partial derivatives can be obtained. Normalization is through

$$\int_{-\infty}^{\infty}\int_{-\infty}^{\infty} p_B(\zeta_x,\zeta_y) \, d\zeta_x \, d\zeta_y = 1$$

4. Slope probability density has been described by Hagfors (1968) through the function $p_s(s,\emptyset)$ where $s = \tan\theta$. This expression is normalized using

$$\int_0^{2\pi}\int_0^{\infty} p_s(s,\emptyset) s \, ds \, d\emptyset = 1$$

where conversion to cylindrical coordinates is made possible through

$$s^2 = \zeta_x^2 + \zeta_y^2$$

The density $p_s(s,\emptyset)$ is usually independent of $\emptyset$ and one generally prefers to use

$$p_s'(s) = \int_0^{2\pi} p_s(s,\emptyset)\, d\emptyset$$

5. Comparison of the above functions can begin by equating the integrands of sections 2 and 4 above

$$p_M(\theta,\emptyset) \sin\theta\, d\theta\, d\emptyset = p_s(s,\emptyset) s\, ds\, d\emptyset$$

$$= p_s(\tan\theta,\emptyset) \tan\theta \sec^2\theta\, d\theta\, d\emptyset$$

This leads to

$$p_M(\theta,\emptyset) = \sec^3\theta\, p_s(\tan\theta, \emptyset)$$

From sections 2 and 4 we also have

$$p_p(\theta) = \int_0^{2\pi} p_M(\theta,\emptyset)\, d\emptyset)$$

and

$$p_{s'}(\tan\theta) = \int_0^{2\pi} p_s(\tan\theta,\emptyset)\, d\emptyset$$

so that

$$p_p(\theta) = 2\pi\, p_M(\theta,\phi)$$

$$= 2\pi \sec^3\theta\, p_s(\tan\theta,\phi)$$

$$= \sec^3\theta\, p_{s'}(\tan\theta)$$

From sections 1 and 2 we have, respectively,

$$2\pi \int_0^{\pi/2} p_H(\theta) \sin\theta\, d\theta = 1$$

and

$$\int_0^{\pi/2} p_p(\theta) \sin\theta\, d\theta = 1$$

From these one obtains

$$p_p(\theta) = 2\pi\, p_H(\theta)$$

and thus

$$p_H(\theta) = \sec^3\theta\, p_s(\tan\theta,\phi)$$

$$= \frac{\sec^3\theta}{2\pi}\, p_{s'}(\tan\theta)$$

Finally, from section 1, we have

$$p_H(\theta) = \cos\theta \; p_{RHM}(\theta)$$

so that

$$p_{RHM}(\theta) = \sec^4\theta \; p_s(\tan\theta, \phi)$$

$$= \frac{\sec^4\theta}{2\pi} \; p_{s'}(\tan\theta)$$

We can also equate the integrands of sections 3 and 4, so that

$$p_B(\zeta_x, \zeta_y) \, d\zeta_x \, d\zeta_y = p_s(s,\phi) s \, ds \, d\phi$$

$$= p_s(\tan\theta, \phi) \tan\theta \sec^2\theta \, d\theta \, d\phi$$

In this case, the conversion between (ζ_x, ζ_y) coordinates and (s,ϕ) coordinates is straightforward and

$$p_s(\tan\theta, \phi) = p_B(\zeta_x, \zeta_y)$$

where

$$\zeta_x^2 + \zeta_y^2 = \tan^2\theta$$

6. Radar cross section can be obtained in several ways. Following the notation of section 1, we can denote power intercepted by a facet as

$$P_i \, dA \cos i$$

where P_i is power density in the incoming plane wave and i is angle of incidence on the facet.

This power is reflected into the forward direction with density P_i. But direction of the normal to dA is uncertain by an amount $d\omega$ so the direction of the reflected ray(s) is uncertain by

$$d\omega_r = 4 \cos i \, d\omega$$

At a distance r_{sr} from the facet, that means power can be spread over an area

$$d\omega_r \, r_{sr}^2$$

The expected power density at a receiving antenna, if $\hat{n}$ is uniformly distributed over $d\omega$ and geometry is not otherwise too perverse, is

$$\frac{P_i \, dA \cos i}{d\omega_r r_{sr}^2}$$

The radar equation gives expected power from a receiving antenna of aperture A_R as

$$P_R = \frac{P_i \, \sigma}{4\pi r_{sr}^2} A_R$$

thus

$$\frac{P_i \sigma}{4\pi r_{sr}^2} A_R = \frac{P_i \, dA \cos i}{d\Omega_r \, r_{sr}^2} A_R$$

and

$$\sigma = 4\pi \cos i \frac{dA}{d\Omega_r}$$

Substitution for dA and $d\Omega_r$ gives

$$\sigma_o = \pi p_{RHM} (\theta)$$

where the conversion to radar cross section per unit area of the mean surface is straightforward.

Radar cross section can also be expressed in terms of other density functions as

$$\sigma_o = \pi \sec^4 \theta \, p_s (\tan \theta, \phi)$$

$$\sigma_o = \frac{\sec^4 \theta}{2} p_s' (\tan \theta)$$

$$\sigma_o = \pi \sec \theta \, p_H (\theta)$$

$$\sigma_o = \frac{\sec \theta}{2} p_p (\theta)$$

$$\sigma_o = \pi \sec^4 \theta \, p_B (\zeta_x, \zeta_y)$$

The last expression above is identical to the one derived by Barrick (1968) for scattering from a gently undulating surface.

7. Gaussian Surfaces are among the most easily handled mathematically. Beckmann (1963) uses a gaussian height distribution and gaussian surface auto-correlation function to arrive at a slope density function of the form

$$p_B(\zeta_x, \zeta_y) = \frac{1}{2\pi\zeta_{x_o}^2} \exp\left\{-\frac{\zeta_x^2 + \zeta_y^2}{2\zeta_{x_o}^2}\right\}$$

where $\zeta_{x_o}^2$ is the unidirectional rms slope. This converts directly to

$$p_s(\tan\theta, \phi) = \frac{1}{2\pi\zeta_{x_o}^2} \exp\left\{-\frac{\tan^2\theta}{2\zeta_{x_o}^2}\right\}$$

and thence to

$$p_{s'}(\tan\theta) = \frac{1}{\zeta_{x_o}^2} \exp\left\{-\frac{\tan^2\theta}{2\zeta_{x_o}^2}\right\}$$

From section 5 these can be rewritten to give

$$p_{RHM}(\theta) = \frac{\sec^4\theta}{2\pi\zeta_{x_o}^2} \exp\left\{-\frac{\tan^2\theta}{2\zeta_{x_o}^2}\right\}$$

$$p_H(\theta) = \frac{\sec^3\theta}{2\pi\zeta_{x_o}^2} \exp\left\{-\frac{\tan^2\theta}{2\zeta_{x_o}^2}\right\}$$

$$p_p(\theta) = \frac{\sec^3\theta}{\zeta_{x_o}^2} \exp\left\{-\frac{\tan^2\theta}{2\zeta_{x_o}^2}\right\}$$

Radar cross sections per unit area for the above density functions are

$$\sigma_{o_{RHM}}(\theta,\phi) = \frac{\sec^4\theta}{2\zeta_{x_o}^2} \exp\left\{-\frac{\tan^2\theta}{2\zeta_{x_o}^2}\right\}$$

$$= \sigma_{o_s}(\theta,\phi) = \sigma_{o_H}(\theta,\phi) = \sigma_{o_{s'}}(\theta) = \sigma_{o_p}(\theta)$$

$$\sigma_{o_B}(\zeta_x,\zeta_y) = \frac{\sec^4\theta}{2\zeta_{x_o}^2} \exp\left\{-\frac{\zeta_x^2 + \zeta_y^2}{2\zeta_{x_o}^2}\right\}$$

Dual argument cross sections are those derived from density functions requiring normalization over two variables; single argument cross sections are those from density functions requiring normalization over only one variable. In either case, σ_o must be integrated over all space if total scattered power is desired.

8. Root mean square slope can be computed in a number of ways. The easiest is by using

$$s_o = \left[\int_o^\infty s^2\, p_{s'}(s)\, s\, ds\right]^{1/2}$$

For the density function $p_{s'}(s)$ given in section 7, this leads to an adirectional rms slope, or tilt, of

$$s_o = \sqrt{2}\,\zeta_{x_o}$$

For Parker's density function, the adirectional rms slope is obtained using

$$s_o = \left[\int_0^{\pi/2} \tan^2\theta \; p_p(\theta) \; \sin\theta \; d\theta \right]^{1/2}$$

One also obtains

$$s_o = \sqrt{2} \; \zeta_{x_o}$$

when the function of section 7 is inserted.

For the other density functions, adirectional rms slope can be found from

$$s_o = \left[\int_0^{2\pi} \int_0^{\infty} s^2 \; p_s(s,\phi) \; s \; ds \; d\phi \right]^{1/2}$$

$$s_o = \left[2\pi \int_0^{\pi/2} \tan^2\theta \; p_{RHM}(\theta) \cos\theta \sin\theta \; d\theta \right]^{1/2}$$

$$s_o = \left[2\pi \int_0^{\pi/2} \tan^2\theta \; p_H(\theta) \sin\theta \; d\theta \right]^{1/2}$$

$$s_o = \left[\int_0^{2\pi} \int_0^{\pi/2} \tan^2\theta \; p_M(\theta,\phi) \sin\theta \; d\theta \; d\phi \right]^{1/2}$$

$$s_o = \left[\int_{-\infty}^{\infty} \int_{-\infty}^{\infty} (\zeta_x^2 + \zeta_y^2)\, p_B(\zeta_x, \zeta_y)\, d\zeta_x\, d\zeta_y \right]^{1/2}$$

For an isotropic surface, having the same statistics in x and y directions and independent slopes ζ_x and ζ_y, the last of the above expressions may be written

$$s_o = \sqrt{2} \left[\int_{-\infty}^{\infty} \zeta_x^2\, p_{B'}(\zeta_x)\, d\zeta_x \right]^{1/2}$$

where $p_{B'}(\zeta_x)$ is the one dimensional analog of $p_B(\zeta_x, \zeta_y)$:

$$p_B(\zeta_x, \zeta_y) = p_{B'}(\zeta_x)\, p_{B'}(\zeta_y)$$

In practice, values of radar cross section as a function of incidence angle are used to determine the corresponding probability density function according to the relationship of section 6. Rms slope then is obtained as in this section above.

REFERENCES APPEARING SOLELY IN THE APPENDIX

Barrick, D.E., Rough surface scattering based on the specular point theory, IEEE Trans. on Ant. and Prop., AP-16, 449-454, 1968.

Beckmann, P., "Part I - Theory" in Beckmann and Spizzichino, 1963.

Hagfors, T., Chapter 4 - Relations between rough surfaces and their scattering properties as applied to radar astronomy, in Evans and Hagfors, 1968.

Muhleman, D.O., Radar scattering from Venus and the moon, Astron. J., 69, 34-41, 1964.

Parker, M.N., Radio-wave scattering from rough surfaces and the estimation of surface shape, Stanford Electronics Laboratories, report SEL-73-041, Stanford, CA, 1973.

Rea, D.G., N. Heatherington and R. Mifflin, The analysis of radar echoes from the moon, J. Geophys. Res., 69, 5217-5223, 1964.

Rea, D.G., N. Heatherington and R. Mifflin, A note on 'The analysis of radar echoes from the moon', J. Geophys. Res., 70, 1565, 1965.

TABLE I

TERRAIN CLASSIFICATION ALONG APOLLO 15 GROUND TRACK

Highlands	
41°E and east	Cratered terrain
29-35°E	Mons Argaeus and environs
1-7°E	Montes Apenninus
Maria	
37-39°E	Mare Tranquilitatis
9-27°E	Mare Serenitatis
9-35°W	Mare Imbrium (except Euler)
35-67°W	Mare Procellarum
Other	
39-41°E	Transition between maria and highlands
35-37°E	
27-29°E	
7-9°E	
7-9°W	
0°	Three-way transition: Apennine Bench, Palus Putredinis (mare), Montes Apenninus
1-7°W	Apennine Bench
29°W	Euler (crater)
67°W and west	Outlier from cratered terrain

TABLE II

WAVELENGTH DEPENDENCE IN LUNAR SCATTERING

APOLLO 15 13 VS 116 CM

AREA	LONGITUDE	LATITUDE	N	$\bar{S}$	$\bar{\alpha}$
MARE TRANQUILITATIS	39-33°E	16-18°N	3	0.85 ± 0.07	-0.07 ± 0.04
MARE SERENITATIS	27-11°E	20-24°N	8	0.65 ± 0.05	-0.20 ± 0.04
MONTES APENNINUS	9- 1°E	24°N	4	0.99 ± 0.08	0.00 ± 0.04
MARE IMBRIUM AND MARE PROCELLARUM	11-67°W	25-12°N	27	0.49 ± 0.09	-0.33 ± 0.08
MARE IMBRIUM	11-37°W	25-22°N	12	0.52 ± 0.07	-0.30 ± 0.06
MARE PROCELLARUM	51-67°W	18-12°N	8	0.40 ± 0.04	-0.42 ± 0.05

$$^{*}\text{SLOPE RATIO} = S = \left[\frac{\text{SLOPE AT 116 CM}}{\text{SLOPE AT 13 CM}}\right]^{\alpha} = \frac{116\text{ CM}}{13\text{ CM}}$$

**THESE DATA GROUPINGS ARE SUBSETS OF THE N = 27 MARE IMBRIUM AND MARE PROCELLARUM GROUP IMMEDIATELY ABOVE

FIGURE CAPTIONS

1. (a) Fit error between experimental surface slope probability density functions and gaussian (+), exponential (x), and Hagfors (solid line) theoretical curves. Hagfors is somewhat better than the exponential; both are considerably better than the gaussian. (b) RMS surface roughness appropriate to best fit Hagfors law along Apollo 15 ground track at 13 cm wavelength.

2. Examples of good fits along the Apollo 16 ground track to each of the three theoretical expressions considered. Error bars refer to uncertainty in the data points and not to the fit between data and theoretical curves.

3. "Phase diagram" used to show data behavior with regard to each theoretical scattering law. Distance from a vertex is based on the square error in the fitting process; the constant K is chosen to satisfy the identity. In the figure, ε_H^2 is less than either ε_G^2 or ε_E^2 (indicating that the Hagfors law provides the best fit) so that D_H is less than either D_G or D_E and the point is closest to the Hagfors vertex.

4. "Phase diagram" showing all 13 cm wavelength Apollo 15 points. Most surface slope probability density functions show best agreement with the Hagfors law; a lesser number show best agreement with the exponential, and the least number show best agreement with the gaussian. Histograms show distribution of points when only two scattering laws are compared.

5. "Phase diagram" for 13 cm Apollo 15 points in maria. When highland points are omitted, the distribution moves away from the gaussian scattering law.

6. "Phase diagram" for 13 cm Apollo 15 points in highlands. Consideration of highland data only shows Hagfors preferred but with a shift away from the exponential and toward the gaussian.

7. Fit error (a) and Hagfors law rms surface slope (b) from Apollo 15 data at 116 cm wavelength. Fit error shows same behavior as at 13 cm (see Fig. 1); surface roughness is noticeably lower in maria but similar in highlands. Sharp spike near 30°W longitude results from very irregular terrain around the crater Euler.

8. Ratio of roughness estimates at 116 cm to those at 13 cm along the Apollo 15 ground track (see Table II).

FIG. 1

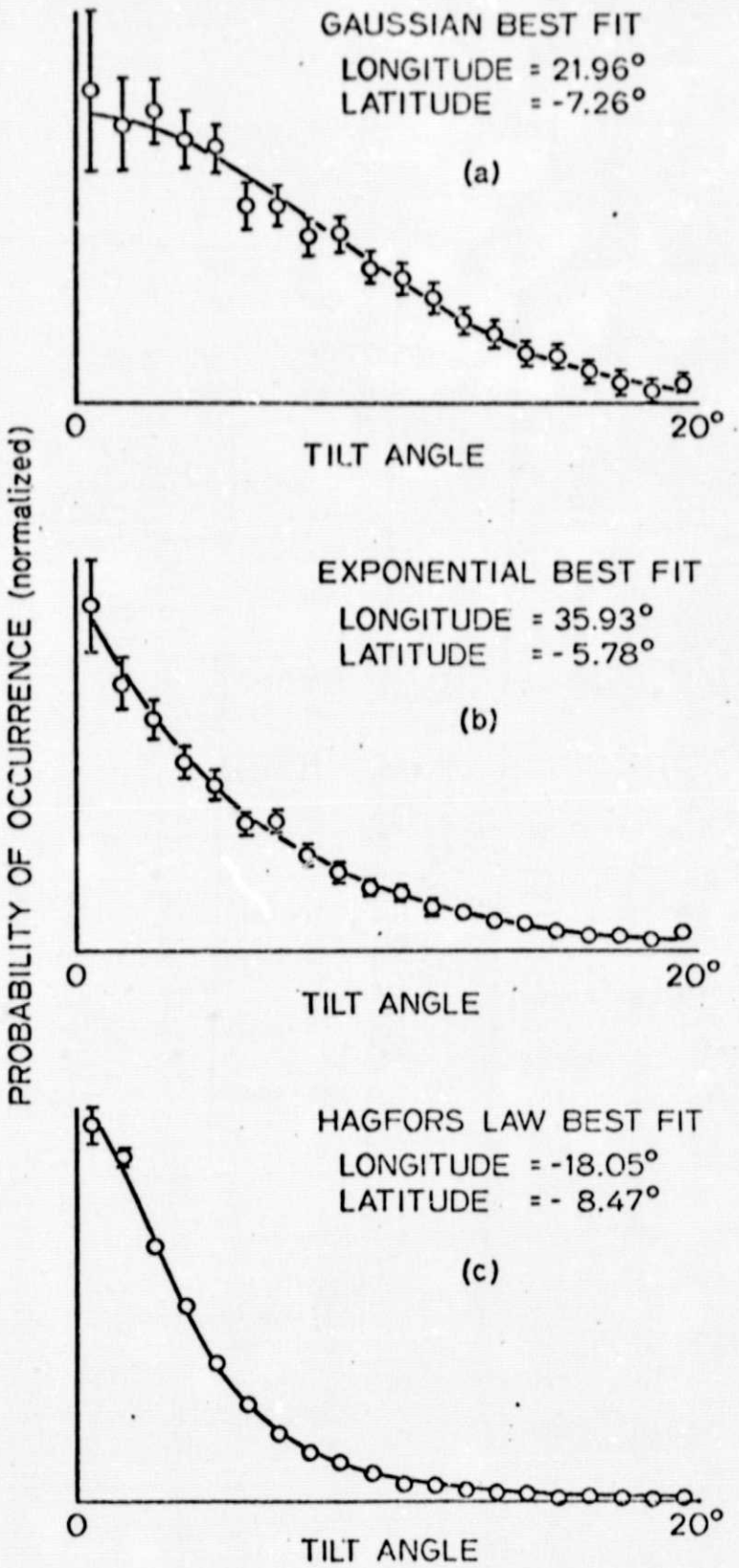
GAUSSIAN BEST FIT
LONGITUDE = 21.96°
LATITUDE = -7.26°
(a)
0
20°
TILT ANGLE
PROBABILITY OF OCCURRENCE (normalized)
EXPONENTIAL BEST FIT
LONGITUDE = 35.93°
LATITUDE = - 5.78°
(b)
0
20°
TILT ANGLE
HAGFORS LAW BEST FIT
LONGITUDE = -18.05°
LATITUDE = - 8.47°
(c)
0
20°
TILT ANGLE

FIG. 2

$$\frac{K}{\epsilon_H^2} + \frac{K}{\epsilon_E^2} + \frac{K}{\epsilon_G^2} = 1$$

$D_H = 100\,(1 - K/\epsilon_H^2)$

$D_E = 100\,(1 - K/\epsilon_E^2)$

$D_G = 100\,(1 - K/\epsilon_G^2)$

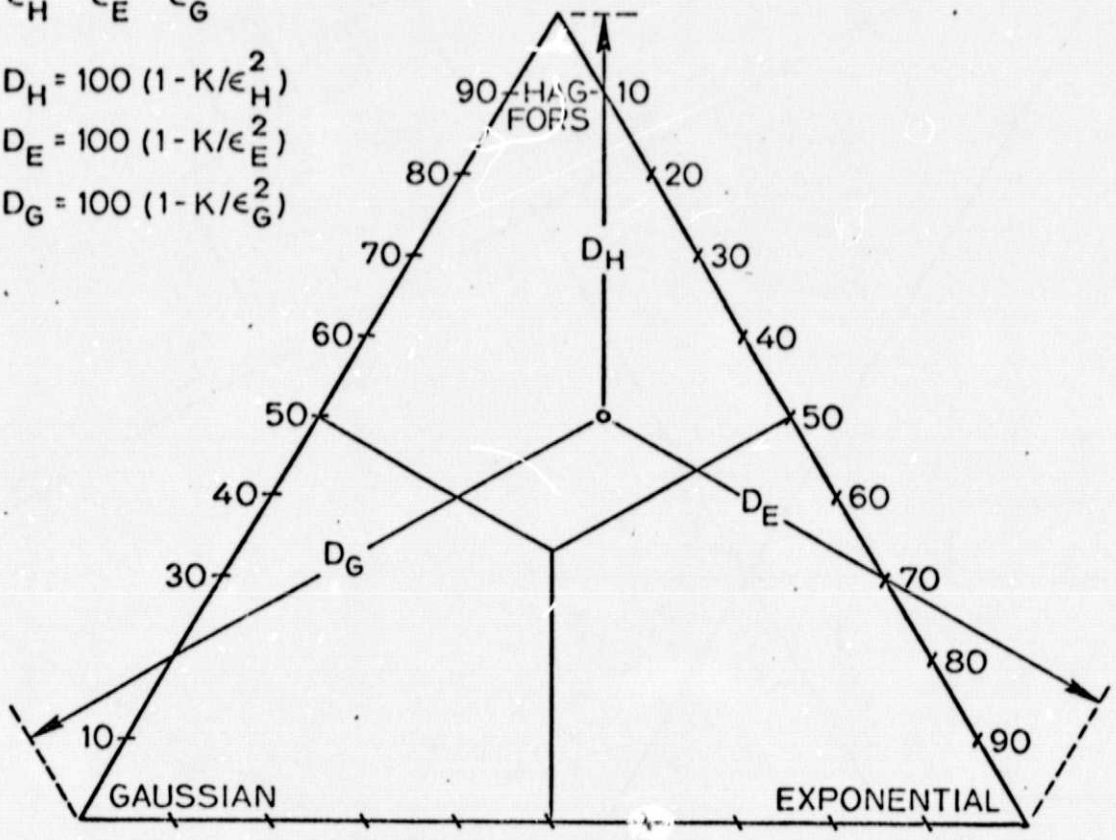

FIG. 3

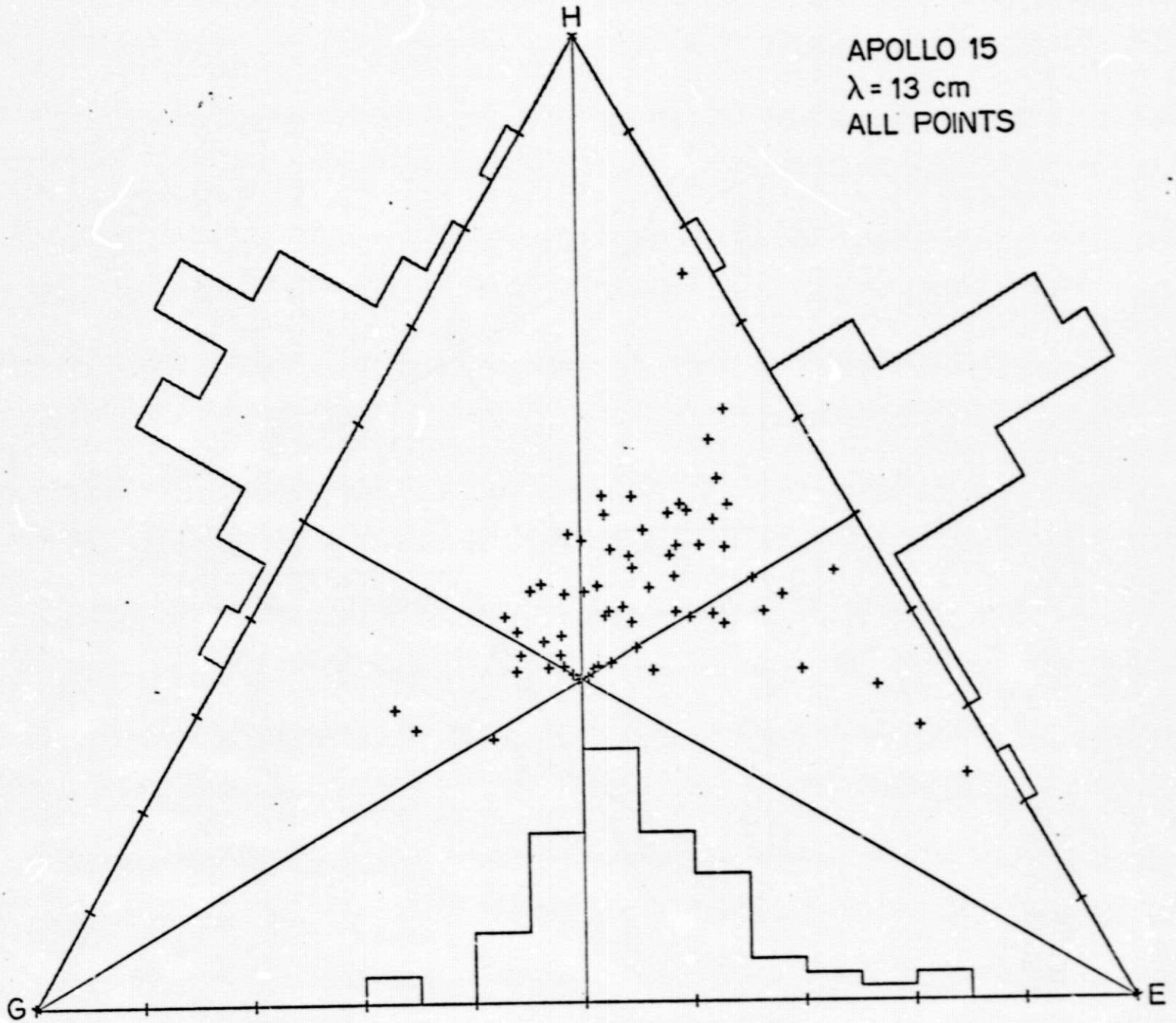

FIG. 4

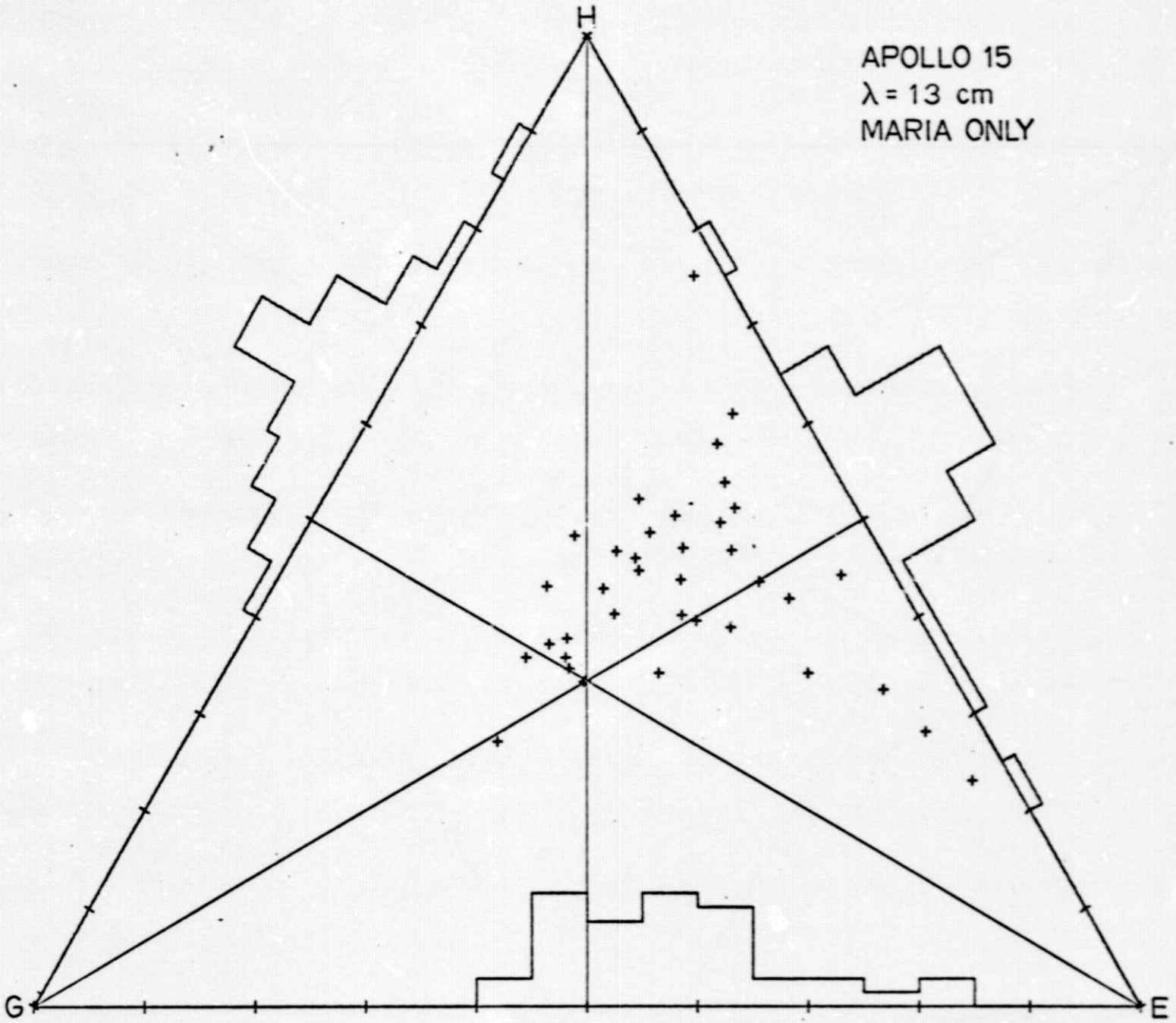

FIG. 5

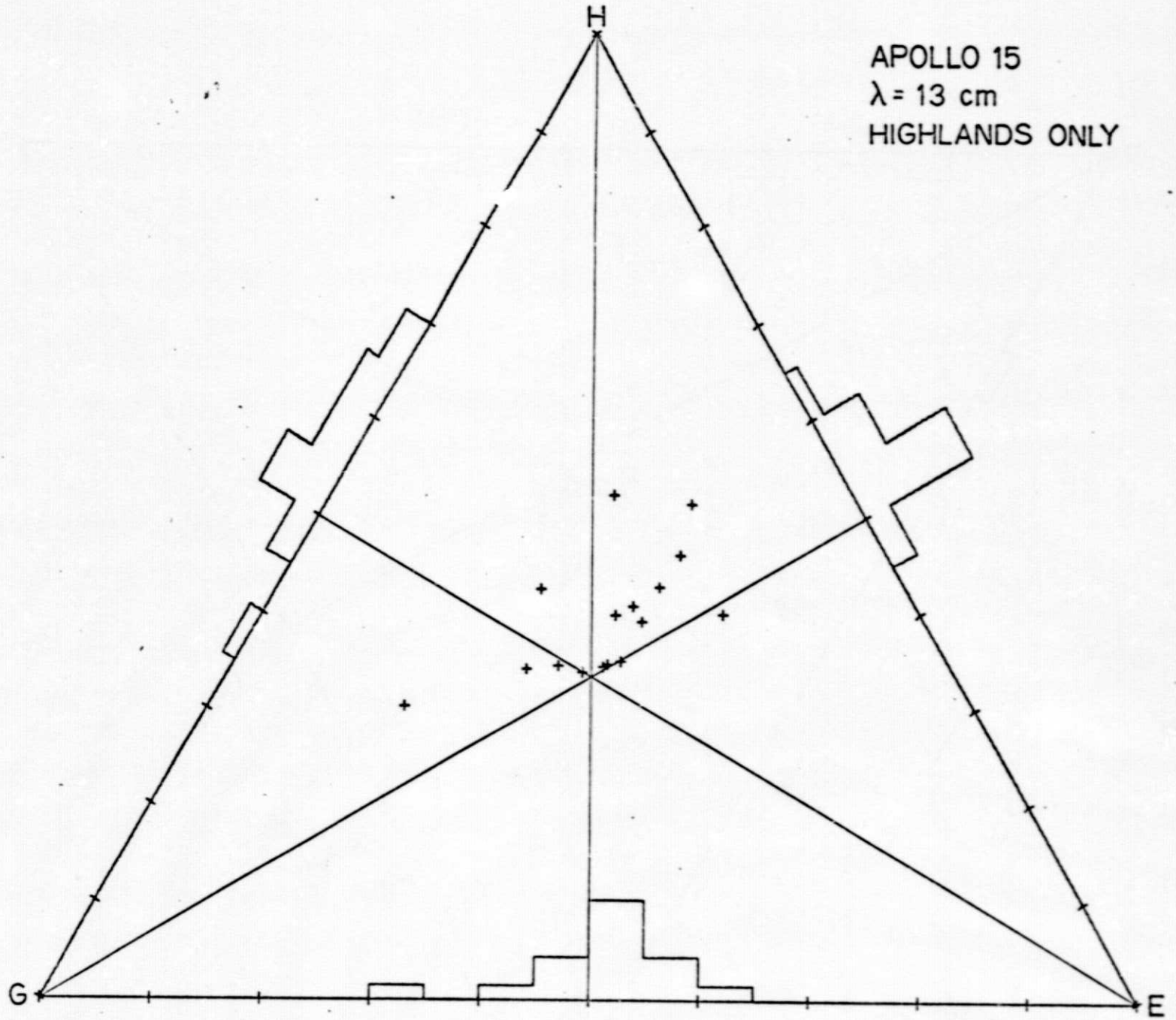
H
G
E
APOLLO 15
λ = 13 cm
HIGHLANDS ONLY

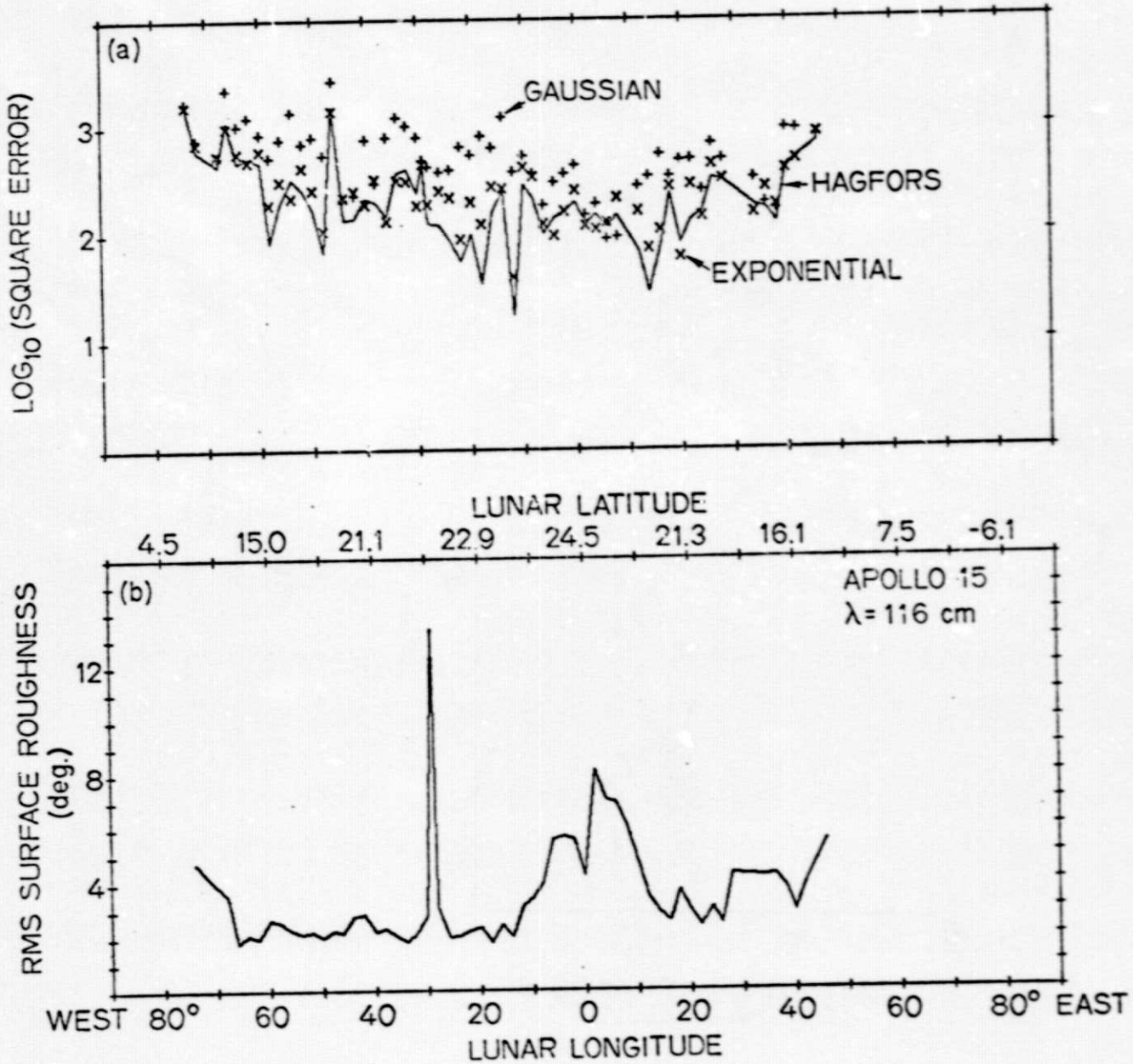
(a)
GAUSSIAN
HAGFORS
EXPONENTIAL
LOG10 (SQUARE ERROR)
3
2
1
LUNAR LATITUDE
4.5
15.0
21.1
22.9
24.5
21.3
16.1
7.5
-6.1
(b)
APOLLO 15
λ = 116 cm
RMS SURFACE ROUGHNESS (deg.)
12
8
4
WEST
80°
60
40
20
0
20
40
60
80°
EAST
LUNAR LONGITUDE

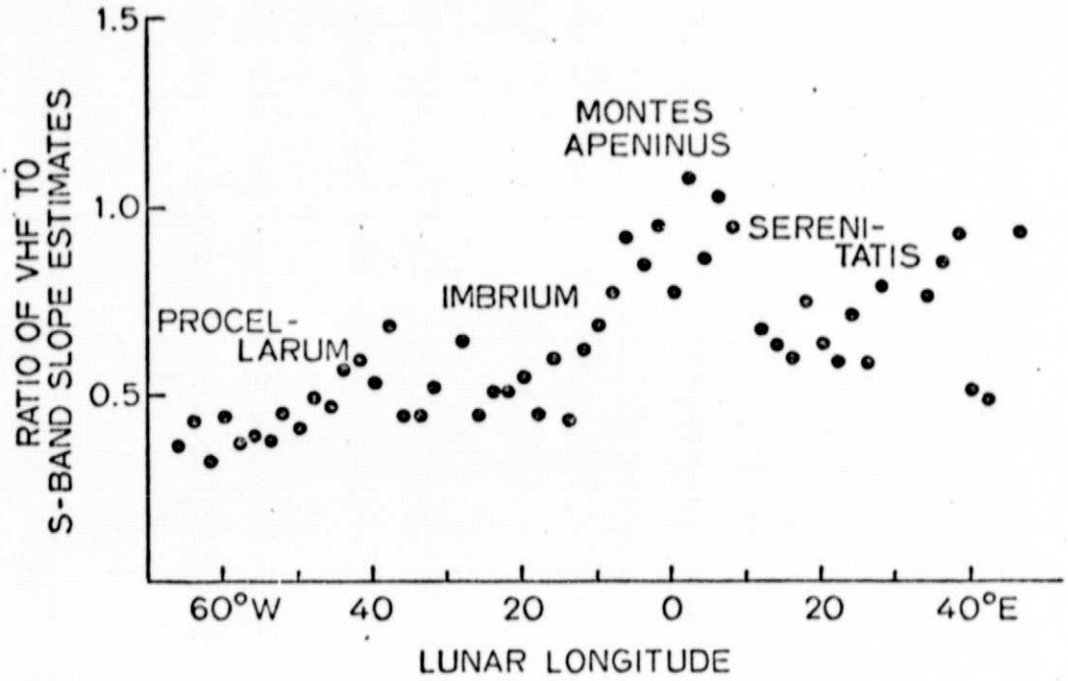
1.5
1.0
0.5
RATIO OF VHF TO
S-BAND SLOPE ESTIMATES
MONTES
APENINUS
SERENI-
TATIS
IMBRIUM
PROCEL-
LARUM
60°W
40
20
0
20
40°E
LUNAR LONGITUDE

FIG. 8